PFC/JA-89-23

Prebunching in a Collective Raman
Free Electron Laser Amplifier

J. S. Wurtele, G. Bekefi, R. Chu and K. Xu

April 1989

Department of Physics
Plasma Fusion Center
Research Laboratory of Electronics

Massachusetts Institute of Technology
Cambridge, Massachusetts 02139 USA

# Prebunching in a Collective Raman Free

# Electron Laser Amplifier

J. S. Wurtele, G. Bekefi, R. Chu. and K. Xu

Department of Physics.

Research Laboratory of Electronics,

and

Plasma Fusion Center,

Massachusetts Institute of Technology,

Cambridge, MA 02139

April 5, 1989

1

# Abstract

Experiments, theory, and simulations are reported on the effects of electron prebunching in a mildly relativistic, low current (200 kV, 1A) free-electron laser amplifier operating in the collective (Raman) regime at a frequency of $\sim 10$ GHz. Prebunching is established by injecting an electromagnetic wave into a bifilar helical wiggler and then transporting the bunched beam into a second magnetic wiggler region. The wave growth rate is deduced from measurements of the radiation intensity as a function of interaction length. Observations show that prebunching can increase the radiation growth rate manyfold as compared with a system without prebunching.

# 1   INTRODUCTION

Experimental and theoretical studies [1] of prebunching in free electron lasers (FELs) are normally carried out in the low gain, single particle (Compton) regime applicable to very short radiation wavelengths (visible and ultraviolet) where electron beam energies in excess of several hundred MeV are used. In contrast, our experiments [2] are made at microwave frequencies using mildly relativistic electrons ($\sim$ 200 keV). In this collective (Raman) regime, the gains are high and the effects of space charge cannot be neglected. We find that prebunching increases the growth rate of the radiation dramatically as compared with the case where prebunching has not been incorporated. In this paper the experiments are compared with computer simulations and good agreement is obtained. In addition, a simple analytic theory is given.

# 2   EXPERIMENTAL ARRANGEMENT

Fig. 1 shows a schematic of our experiment. The accelerating potential is supplied by a Marx generator (Physics International Pulserad 615 MR, which has a maximum capability of 500 kV and 4 kA). The electron beam is generated by a thermionically emitting, electrostatically focused, Pierce-type

electron gun (250 kV, 250 A) from a SLAC klystron (model 343). An assembly of focusing coils transports the electron beam into the drift tube. To ensure good electron orbits, an aperture is inserted which limits the electron beam radius to $r_b = 0.245$ cm so that only the inner portion of the beam is used . With this precaution, the energy spread of the beam entering the magnetic wiggler is $\Delta\gamma_{\parallel}/\gamma_{\parallel} \leq 0.003$ ($\gamma_{\parallel} = [1 - v_{\parallel}^2/c^2]^{-1/2}$).

The gun focusing coils guide the electron beam into a rectangular (0.40" x 0.90") stainless steel evacuated drift tube which is also the waveguide for the electromagnetic radiation. The beam is contained by a uniform axial magnetic field $B_{\parallel}$ that has a power supply limited maximum of 7 kG.

The 65 period circularly polarized magnetic wiggler has a period $l_w = 3.5$ cm, a maximum amplitude $B_w = 1.0$ kG, and is generated by bifilar conductors. Since the beam aperture limits the size of the beam to $r_b/l_w \approx 0.07$, the wiggler field is close to that of an ideal wiggler. At the wiggler entrance a slowly increasing field amplitude is produced by resistively loading the first six periods of the wiggler magnet.

The 2.7 m long drift tube acts as a rectangular waveguide whose fundamental $TE_{10}$ mode has a cutoff frequency of $\omega_c/2\pi = 6.6$ GHz. Microwaves are launched onto the electron beam by a waveguide coupler (see Fig. 1).

All our measurements are carried out at frequencies between 9 and 11 GHz. At these frequencies the empty waveguide can support only the fundamental ($TE_{10}$) mode, all higher modes being evanescent.

Monochromatic radiation as high as 20 kW is injected into the interaction region via the directional coupler. At low power levels ($\leq 10$ W) we use a CW traveling wave tube as the input source. At higher power levels we use a pulsed ($\sim 1\mu s$) magnetron driver. Because of the low conductivity of the stainless steel waveguide, there is an RF power loss of $\sim 0.9$ dB/m, or a 3 dB loss over the entire system length.

# 3  MEASUREMENTS

The interaction space is divided into two roughly equal lengths by means of a tungsten mesh stretched across the waveguide (see Fig. 1) and placed at an axial distance $z = z^* \simeq 115$ cm from the wiggler entrance. The mesh is almost totally transparent ($\sim 94$ percent) to the electron beam generated to the left of the mesh, but highly reflecting to the electromagnetic radiation incident upon it. Thus, the left-hand side can be viewed as the prebunching region where spatially growing bunches are induced by the conventional FEL

mechanism. The bunched beam then traverses the mesh almost unhindered and immediately interacts with the weak electromagnetic wave that has been allowed to pass through the mesh. (The mesh attenuation of the wave incident from the left equals 20.0 dB.) Beyond the mesh the electromagnetic wave grows spatially, and additional bunching also occurs. In this region, an enhanced wave growth rate is expected, because the electrons enter pre-bunched. The use of the mesh rather than an RF attenuator of finite axial extent, as is common in TWT's [3], minimizes the possibility of debunching with distance, as may well occur as a result of space charge repulsion and/or Landau damping of the pondermotive wave.

At the output end of the wiggler, a mica window transmits the linearly polarized radiation generated in the drift tube, where it is measured by means of standard calibrated crystal detectors. In order to determine the growth rate of the wave, the output intensity must be measured as a function of the length of the interaction region. This is accomplished by means of an axially movable horseshoe "kicker" magnet that deflects the electron beam into the waveguide wall at any desired position $z$, thereby terminating the interaction at that point. The position $z$ can be chosen to be to the left or to the right of the tungsten mesh (situated at $z = z^* \simeq 115$ cm).

6

Fig. 2 shows how the RF power output $P$ measured at the far downstream end varies with the "kicker" magnet position $z$, for two different values of the wiggler strength $B_w$. As a result of prebunching, we see that to the right of the mesh the power rises much more rapidly with $z$ than to the left of the mesh. The phenomenon is quite dramatic. For example, in the case of the $B_w = 188$ G wiggler field, the radiation growth rate $\Gamma(z < z^*) \equiv (1/P)dP/dz$ equals 6.9 dB/m, whereas to the right of the mesh, $\Gamma(z > z^*) = 32$ dB/m. Note, however, that for our parameters the gain $G$, namely the ratio of total output power to the total injected power (at $z = 0$), is somewhat less relative to what $G$ would have been in the absence of the mesh. The reason is the 20 dB loss due to the mesh which has not been made up by the increased growth rate $\Gamma$ at $z > z^*$.

Fig. 3 shows how the power $P(z)$ varies with $z$ for three different values of the input power $P_{in}$ ranging from 0.3 to 40 W. The wiggler strength $B_w$ is the same for all three values of $P_{in}$. It is seen that the growth rate $\Gamma$ (given by the slopes of the curves) are virtually independent of the input power.

Fig. 4 illustrates the time history of our FEL as observed on an oscilloscope screen. Since our Marx accelerator has an RC droop, the electron beam energy sweeps through a range of values as seen in Fig. 4a. Thus, in

7

a single shot one observes the entire range of FEL interactions as a function of electron beam energy. Fig. 4b shows how the power output varies with beam energy at $z < z^*$ when a monochromatic, CW signal is injected into the interaction region via the wave launcher (see Fig. 1). Amplification occurs at a time during the voltage pulse corresponding to the resonant intereaction between the injected electromagnetic wave and the slow (negative energy) space charge wave on the beam. At a later time wave damping is seen to occur corresponding to the interaction between the electromagnetic and fast (positive energy) space charge wave. Fig. 4c shows the behavior to the right of the mesh $z > z^*$. We see that the absorption dip in Fig. 4b now appears as a gain peak in 4c.

# 4  THEORY AND SIMULATIONS

A simulation code which will be described in an upcoming paper [4] is used to simulate the experiments. The computer code utilizes an extended one dimensional model to track the nonlinear electron motions in the $(\gamma, \psi)$ space. Instead of assuming a helical wiggler field with constant amplitude, the code includes Bessel functions in the wiggler field to generate more realistic elec-

tron orbits. The presence of an axial magnetic field and RF space charge are also included. The signal power is then given by the self-consistent coupling between the electron beam and the fundamental $TE_{10}$ mode.

Figs. 5 and 6 show the computer simulations of the experimental results shown in Figs. 2 and 3a. The simulations and the experiments can be seen to be in good agreement. Fig. 7 shows the simulations of the experimental results shown in Figs. 4b and 4c. The simulations show that the absorption dip in the prebunching section turns into a gain peak in the section to the right of the mesh, just as observed in the experiments.

The dramatic increase in the radiation growth rate $\Gamma$ is a direct result of prebunching. But in order to understand the phenomenon quantitively, a simple analytic theory is derived. This theory will then be shown to give results that are in excellent agreement with simulations.

Before the equations of motion are stated, it is convenient to introduce the dimensionless field variable

$$a = \frac{\sqrt{PZ_0}}{mc^2/e} e^{i\phi},  \tag{1}$$

where $\phi(z)$ is the phase shift due to the FEL interaction. $P$ is the RF power and $Z_0 = \sqrt{\mu_0/\varepsilon_0}$ is the characteristic impedance of vacuum. An appropriate

length scale is defined as

$$C = \sqrt{\frac{\omega}{ck_z ab}},$$  (2)

where $a$ and $b$ are the linear dimensions of the rectangular waveguide, $\omega$ the

radiation frequency and $k_z$ the axial wave number.

The general equations of motion [4] hold in both sections to the left and

to the right of the mesh. For simplicity and clarity these equations are

written in complex forms in terms of the relativistic energy factor $\gamma_j$ and the

normalized axial $\beta_{\parallel j}$ and transverse $\beta_{\perp j}$ velocities of the jth particle as,

$$\frac{d\gamma_j}{dz} = \frac{iC\beta_{\perp j}}{2\beta_{\parallel j}} a e^{i\theta_j} - \frac{i\omega_{p0}^2 f_{sc}^2}{c^2(k_z + k_w)} e^{i\theta_j} \left\langle e^{-i\theta} \right\rangle + c.c.,$$  (3)

$$\frac{d\theta_j}{dz} = k_w + k_z - \frac{\omega}{c\beta_{\parallel j}},$$  (4)

$$\frac{da}{dz} = \frac{iCI}{2I_A} \left\langle \frac{\beta_{\perp}}{\beta_{\parallel}} e^{-i\theta} \right\rangle.$$  (5)

$\omega_{p0}$ is the nonrelativistic plasma frequency,

$$\omega_{p0} = \sqrt{\frac{Z_0 eI}{m\pi r_e^2 \beta_{\parallel 0}}}.$$  (6)

with $I$ as the beam current, $r_e$ the beam radius and $I_A = 17kA$ the Alfen

current; the space charge reduction factor $f_{sc} \sim 0.5$ [4] for the parameters of

our experiments.

First we consider the section to the left of the mesh $(z < z^*)$ where normal

FEL interactions with no prebunching take place. For simplicity a cold beam is assumed. The linearization proceeds by defining

$$\Delta k \;=\; k_w + k_z - \frac{\omega}{c\beta_{\|0}}, \tag{7}$$

$$\gamma_j \;=\; \gamma_0 + \delta\gamma_j, \tag{8}$$

$$\theta_j \;=\; \theta_{j0} + \Delta k z + \delta\theta_j, \tag{9}$$

$$\eta \;=\; \frac{CI}{2I_A}, \tag{10}$$

$$\eta_{\|} \;=\; \frac{\omega_{p0}^2 f_{sc}^2}{c^2(k_w + k_z)}. \tag{11}$$

$\Delta k$ is the detuning parameter; $c\beta_{\|0}$ is the initial axial velocity; $\gamma_0$ is the initial energy and $\theta_{j0}$ is the initial phase of the jth electron. It follows that, at $z = 0$, $\delta\gamma_j = \delta\theta_j = 0$.

With the injected beam unbunched, the zero'th average vanishes,

$$\left\langle e^{-i(\theta_0 + \Delta k z)} \right\rangle = 0, \tag{12}$$

and the linearized equations are

$$\frac{d\delta\gamma_j}{dz} \;=\; \frac{iC\beta_{\perp 0}}{2\beta_{\|0}} a e^{i(\theta_{j0} + \Delta k z)} - \eta_{\|} \left\langle \delta\theta e^{-i(\theta_0 + \Delta k z)} \right\rangle e^{i(\theta_{j0} + \Delta k z)} + c.c., \tag{13}$$

$$\frac{d\delta\theta_j}{dz} \;=\; \frac{\omega}{c\beta_{\|0}^2} \frac{\partial\beta_{\|0}}{\partial\gamma} \delta\gamma_j, \tag{14}$$

$$\frac{da}{dz} \;=\; \frac{\eta\beta_{\perp 0}}{\beta_{\|0}} \left\langle \delta\theta e^{-i(\theta_0 + \Delta k z)} \right\rangle. \tag{15}$$

11

Exponential forms for the perturbations are then assumed.

$$\delta \gamma_j = \sum_s \overline{\delta \gamma_s} e^{i(\theta_{j0} + \Delta k z + \alpha_s z)} + c.c., \qquad (16)$$

$$\delta \theta_j = \sum_s \overline{\delta \theta_s} e^{i(\theta_{j0} + \Delta k z + \alpha_s z)} + c.c., \qquad (17)$$

$$a = \sum_s \overline{a_s} e^{i \alpha_s z}, \qquad (18)$$

Substituting the perturbations in Eqs. (16)-(18) into Eqs. (13)-(15) yields the dispersion relation

$$\alpha_s^3 + 2\Delta k \alpha_s^2 + (\Delta k^2 - \frac{\omega}{c\beta_{\parallel 0}^2} \frac{\partial \beta_{\parallel 0}}{\partial \gamma} \eta_{\parallel}) \alpha_s + \frac{C^2 \beta_{\perp 0}^2 \omega I}{4 c \beta_{\parallel 0}^4 I_A} \frac{\partial \beta_{\parallel 0}}{\partial \gamma} = 0 \qquad (19)$$

For peak gain in the Raman regime, $\Delta k >> \alpha_s$; therefore the $\alpha^3$ term in the dispersion relation can be ignored.

We now turn our attention to the section to the right of the mesh ($z > z^*$), the section that starts with a prebunched beam. The co-ordinate system is redefined as $z' = z - z^*$, $z^*$ being the location of the mesh. As before the linearization proceeds by defining

$$\gamma_j' = \gamma_0 + \delta \gamma_j', \qquad (20)$$

$$\theta_j' = \theta_{j0}' + \Delta k z' + \delta \theta_j', \qquad (21)$$

where $\theta_{j0}' = \theta_{j0} + \Delta k z^*$. $\Delta k, \gamma_0$, and $\theta_{j0}$ are defined to be the same quantities used earlier when the prebunching section is considered. $\gamma_0$ and $\theta_{j0}'$ here are

12

not the energy and phase of the jth electron at $z' = 0$. Instead they are the energy and phase of the jth electron there if no FEL interaction (i. e. prebunching) has taken place in the section to the left of the mesh. Therefore $\gamma_0$ and $\theta'_{j0}$ do not contain any information about prebunching. Instead the crucial information is contained in the $\delta\gamma'_j$ and $\delta\theta'_j$ terms at $z' = 0$. Here, $\delta\gamma'_j \neq 0$ and $\delta\theta'_j \neq 0$ at $z' = 0$, in contrast to $\delta\gamma_j = \delta\theta_j = 0$ at $z = 0$.

The perturbations are defined to have exactly the same forms as those in Eqs. (16)-(18),

$$\delta\gamma'_j = \sum_s \overline{\delta\gamma'_s} e^{i(\theta'_{j0}+\Delta k z'+\alpha'_s z')} + c.c., \tag{22}$$

$$\delta\theta'_j = \sum_s \overline{\delta\theta'_s} e^{i(\theta'_{j0}+\Delta k z'+\alpha'_s z')} + c.c., \tag{23}$$

$$a' = \sum_s \overline{a'_s} e^{i\alpha'_s z'}. \tag{24}$$

Since $\theta'_{j0}$ does not contain any information about prebunching, the zero'th average again vanishes,

$$\left\langle e^{-i(\theta'_0+\Delta k z')} \right\rangle = \left\langle e^{-i[(\theta_0+\Delta k z^*)+\Delta k(z-z^*)]} \right\rangle = \left\langle e^{-i(\theta_0+\Delta k z)} \right\rangle = 0. \tag{25}$$

As a result, the linearized equations of motion are the same as those in Eqs. (13)-(15) with the unprimed variables turned into primed variables. The constants, $\Delta k$, $\beta_{\perp 0}$, and $\beta_{\parallel 0}$, are the same in both sets of equations. With

13

the further assumption that the mesh is totally transparent to the electron beam, parameters $\eta_{\parallel}$ and $\eta$ also remain unchanged. Having the same set of equations of motion with identical perturbation forms assumed as before leads one to conclude that the dispersion relation in Eq. (19) also holds in this section. In another words $\alpha_s = \alpha'_s$. The field growth rates $\alpha_s$ of the individual modes are the same in both sections independent of whether the beam is prebunched or not. What does change are the initial relative amplitudes associated with each of the modes. It will be shown later in the paper how this statement is consistent with the overall increase in the radiation growth rate.

The tungsten mesh attenuates the field by a factor of $A$ and leaves $\gamma_j$ and $\theta_j$ unchanged. In the experiments $A = 10$. By equaling the field and particle variables just to the left and to the right of the mesh, one finds

$$\sum_s \bar{a}'_s = \frac{\sum_s \bar{a}_s e^{i\alpha_s z^*}}{A}, \tag{26}$$

$$\sum_s \overline{\delta\gamma}'_s = \sum_s \overline{\delta\gamma}_s e^{i\alpha_s z^*}, \tag{27}$$

$$\sum_s \overline{\delta\theta}'_s = \sum_s \overline{\delta\theta}_s e^{i\alpha_s z^*}. \tag{28}$$

$\overline{\delta\gamma}_s$ and $\overline{\delta\theta}_s$ can be expressed in terms of $\bar{a}_s$. likewise $\overline{\delta\gamma}'_s$ and $\overline{\delta\theta}'_s$ can be expressed in terms of $\bar{a}'_s$. $\bar{a}'_s$ can then be solved in terms of $\bar{a}_s$.

For an free-electron laser operating at peak gain in the Raman regime, $s$ runs from 1 to 2, corresponding to the two complex conjugate waves. Eqs. (26)-(28) reduce to

$$\sum_{s=1}^{2} \bar{a}'_s = \frac{\sum_{s=1}^{2} \bar{a}_s e^{i\alpha_s z^*}}{A}, \tag{29}$$

$$\sum_{s=1}^{2} \frac{\bar{a}'_s}{\alpha_s} = \sum_{s=1}^{2} \frac{\bar{a}_s e^{i\alpha_s z^*}}{\alpha_s}, \tag{30}$$

with $\alpha_1 = iQ$ and $\alpha_2 = -iQ$ where $Q$ is real and positive.

In the section to the left of the mesh ($z < z^*$), the field can be written as

$$a = a_0 \cosh Qz, \tag{31}$$

or in another form,

$$a = \frac{a_0}{2}(e^{Qz} + e^{-Qz}). \tag{32}$$

Solving Eq. (29) and Eq. (30) for $\bar{a}'_s$ gives the field to the right of the mesh ($z > z^*$),

$$a' = a_0(\frac{\cosh Qz^* \cosh Qz'}{A} + \sinh Qz^* \sinh Qz'), \tag{33}$$

or in another form,

$$a' = \frac{a_0}{2} \left\{ \left[\frac{1}{2}(\frac{1}{A} + 1) + \frac{1}{2}(\frac{1}{A} - 1)e^{-2Qz^*}\right] e^{Qz} + \left[\frac{1}{2}(\frac{1}{A} - 1)e^{2Qz^*} + \frac{1}{2}(\frac{1}{A} + 1)\right] e^{-Qz} \right\}. \tag{34}$$

15

As illustrated in Eq. (32), the field starts out with equal amplitudes in both the growing and decaying modes in the prebunching section. After the radiation passes through the mesh, the relative amplitudes between the two modes shift as illustrated in Eq. (34) while the growth rates in respective modes remain unchanged. It can easily be proved that the overall field amplitude growth rate

$$\frac{1}{a'}\frac{da'}{dz} > \frac{1}{a}\frac{da}{dz} \qquad \text{for all } z \qquad (35)$$

as long as $A > 1$. This increase in the overall field growth rate is therefore accounted for not by the increase in the growth rates in individual modes but by the shifting of the relative amplitudes between them. On the other hand it can also be shown that $a' < a$. In fact

$$\frac{a'}{a} \le \frac{1}{2}(\frac{1}{A} + 1) \qquad \text{for all } z. \qquad (36)$$

In conclusion even the dramatic increase in the overall radiation growth rate cannot compensate for the mesh attenuation, and there is always an reduction in overall gain $G$ when this prebunching scheme is employed. Fig. 8 shows the excellent match between analytic results and simulations.

The case for an free-electron laser operating at peak gain in the collective Raman regime is considered above, but the theory can also be applied

16

to parameter regions besides peak gain and to the single particle Compton regime. Phase shift caused by the mesh or introduced externally can also be taken into account by letting $A$ be complex,

$$A = |A|e^{i\Delta\theta}, \qquad \text{where } \Delta\theta \text{ is the phase shift.} \qquad (37)$$

# 5  DISCUSSION

We have reported on the effects of prebunching in a Raman free-electron laser amplifier, and observed large enhancements in the single pass growth rates $\Gamma$. Most of the observations were made using RF drivers that operate either CW or with microsecond long pulses. To verify that the measurements of $\Gamma$ indeed represent single pass gain and are not marred by reflections (due to the presence of the mesh, for example) we also carried out a series of measurements in which the pulse length ($\sim$ 5 ns) of the RF input was shorter than the round-trip pass through the system.

To the left of the mesh ($z < z^*$), the system behaves as one would expect from a conventional FEL operating in the Raman regime. Thus, when the wiggler field strength $B_w$ is increased from 66 to 188 G (Fig. 2), the growth rate $\Gamma(z < z^*)$ increased from 2.4 to $\sim$ 6.9 dB/m, which shows that $\Gamma(z <$

$z^*) \propto B_w$, in agreement with expectations. Also $\Gamma(z < z^*)$ is found to be independent of the input power $P_{in}$ (Fig. 4) for sufficiently low input powers, such that nonlinear pheonomena are unimportant. This is in agreement with conventional FEL theory.

To the right of the mesh $(z > z^*)$ the situation is different. When $B_w$ is increased from 66 to 188 G (a factor of 2.9), $\Gamma(z > z^*)$ increases from 6.3 to 32 dB/m (a factor of 5.1). However, it is noteworthy that the overall gain $G$ of the system is less than what it would have been in the absence of the mesh (i. e. prebunching). Thus, our experimental configuration is useful primarily not to increase gain, but to suppress parasitic oscillations as is common practice in traveling wave tube (TWT) amplifiers [3].

The experimental observations reported in this paper are fully substantiated by computer simulations and analytic studies. Although we have treated only the cold electron beam case analytically, it can be extended to warm beams and the single particle (Compton) regime.

# 6 ACKNOWLEDGMENTS

# References

[1] R. Coisson, "Optical klystrons," in *Particle Accelerators*. New York, NY: Gordon and Breach, 1981, vol. II, pp. 245-253, and references therein.

M. Billardon, P. Elleaume, Y. Lapierre, J.M. Ortega, C. Bazin, M. Bergher, J. Marilleau, and Y. Petrov, "The Orsay storage ring free electron laser: New results," in *Proc. 7th Int. Conf. Free Electron Lasers*, E.T. Scharlemann and D. Prosnitz, Eds. Amsterdam, The Netherlands: North Holland, 1986, pp. 26-34.

G. Vignola, R.R. Freeman, B.M. Kincaid, C. Pellegrini, A. Luccio, J. Murphy, J. Galayda, and A. Van Steenbergen, "A new method for pumping an optical klystron," *Nucl. Instrument. Methods Phys. Res.*, vol. A239, pp. 43-46, 1985.

[2] C. Leibovitch, K. Xu, and G. Bekefi, IEEE J. Quantum Electr. $\underline{24}$, 1825 (1988).

[3] J.R. Pierce, *Traveling Wave Tubes*. Princeton, NJ: Van Nostrand, 1950, ch. IX, pp. 131-144; S.Y. Liao, *Microwave Devices and Circuits*. Englewood Cliffs, NJ: Prentice-Hall, 1985, pp. 220-224.

J. Fajans and J.S. Wurtele, IEEE J. Quantum Electr. $\underline{24}$, 1805 (1988).

[4] J.S. Wurtele, J. Fajans, and R. Chu, "Theory and Experiment of Collective Free Electron Lasers," paper in preparation.

## FIGURE CAPTIONS

**Fig. 1.** Schematic of the experimental setup.

**Fig. 2.** RF power output as a function of interaction length, for two different wiggler field amplitudes $B_w$; RF power input 3 W; RF frequency 10.5 GHz; electron beam energy 170 keV; electron beam current $\sim$ 1 A; axial guide magnetic field $B_{\parallel} = 1.63$ kG.

**Fig. 3.** RF power output as a function of interaction length for three different values of RF input power. RF frequency 9.3 GHz; electron beam energy 130 keV; electron beam current $\sim$ 1 A; wiggler field strength 188 G; axial guide field $B_{\parallel} = 1.63$ kG.

**Fig. 4.** Typical oscilloscope traces showing (a) the beam voltage, (b) the output microwave power when the electron beam is terminated before the mesh $(z < z^*)$ and (c) when it is terminated after the mesh $(z > z^*)$.
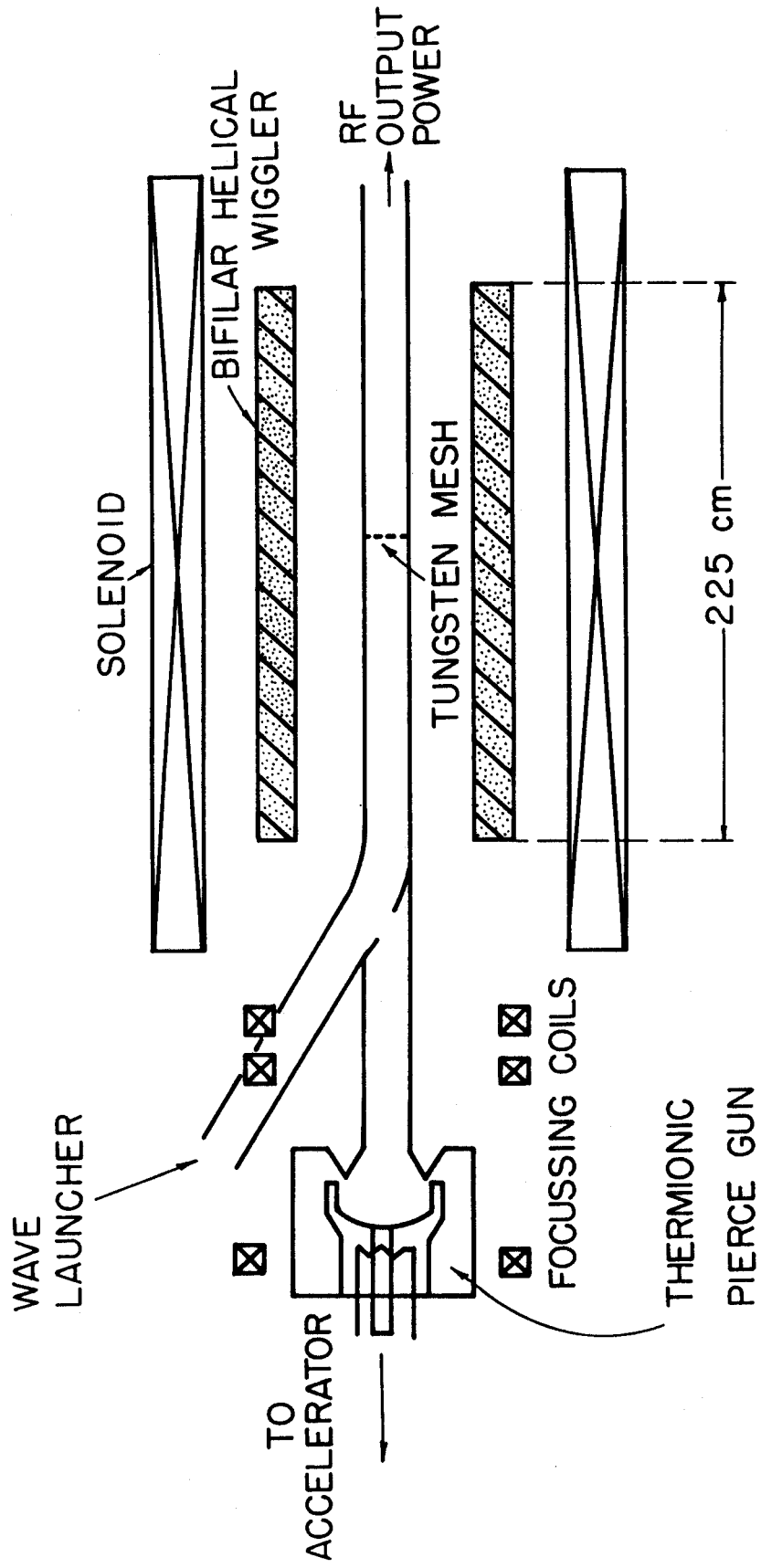
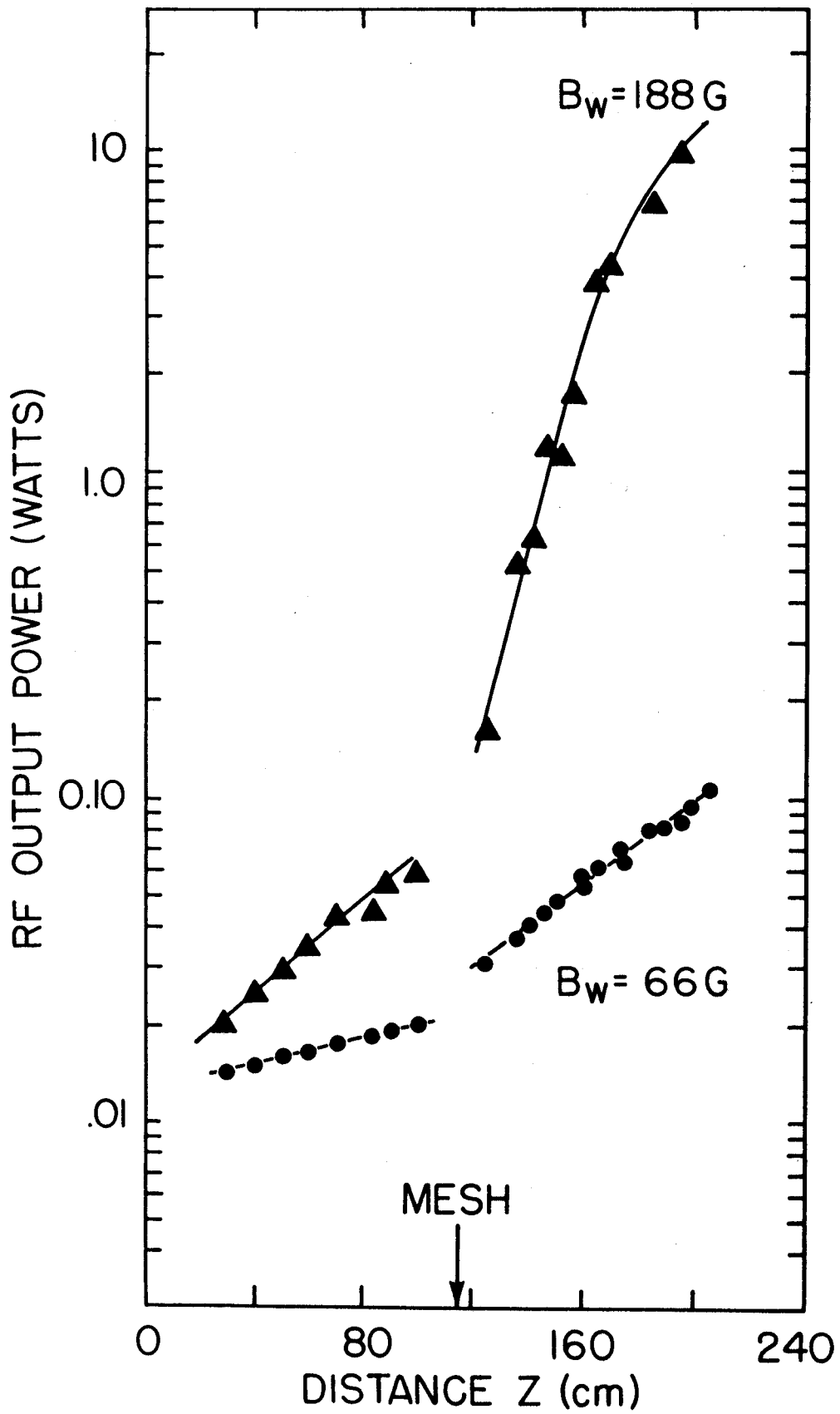**Fig. 5.** Computer simulations of the experimental results shown in Fig. 2.

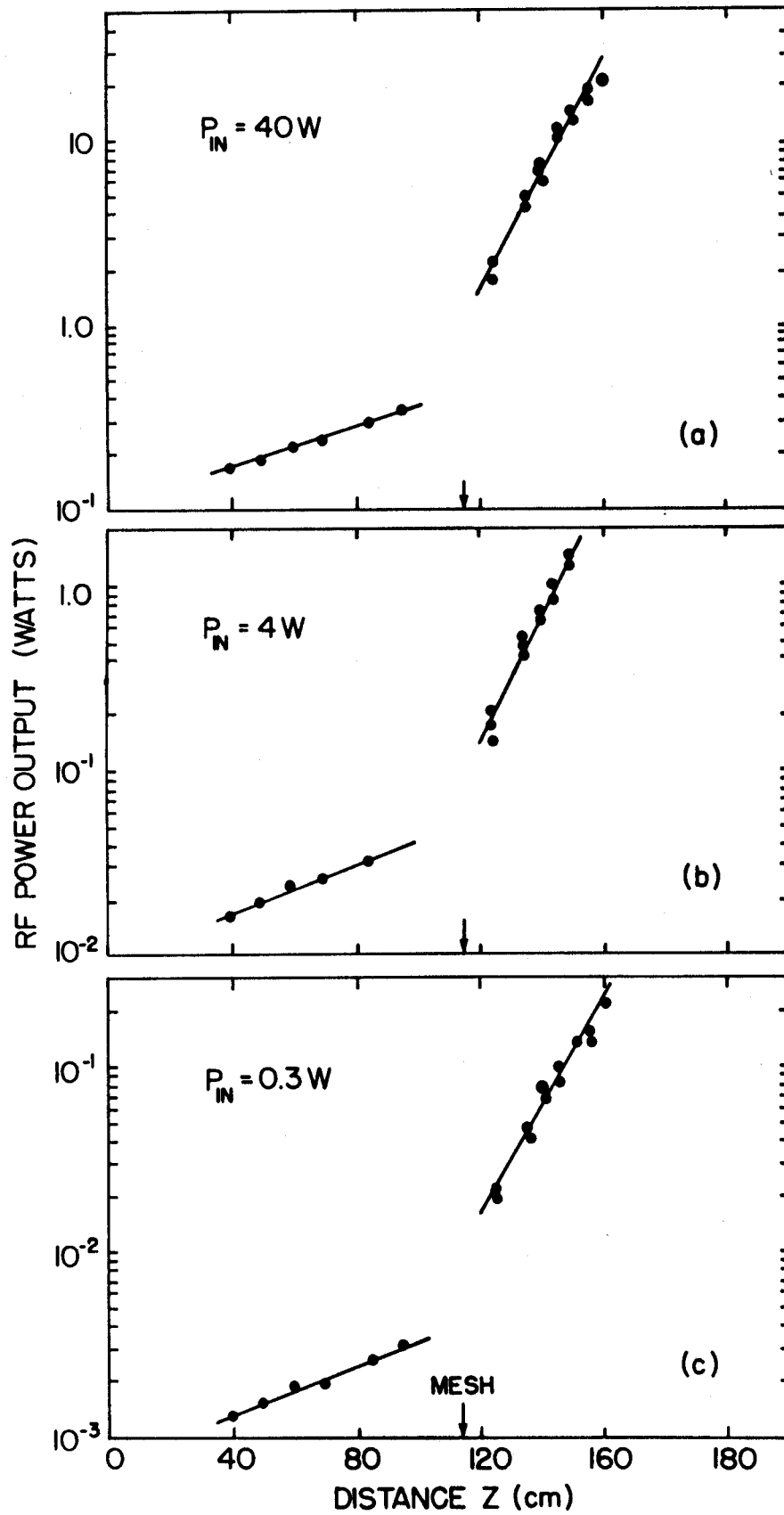**Fig. 6.** Computer simulations of the experimental results shown in Fig. 3a.

**Fig. 7.** Computer simulations of the experimental results shown in Figs. 4b,c. Note that in making the comparison, the electron beam energy
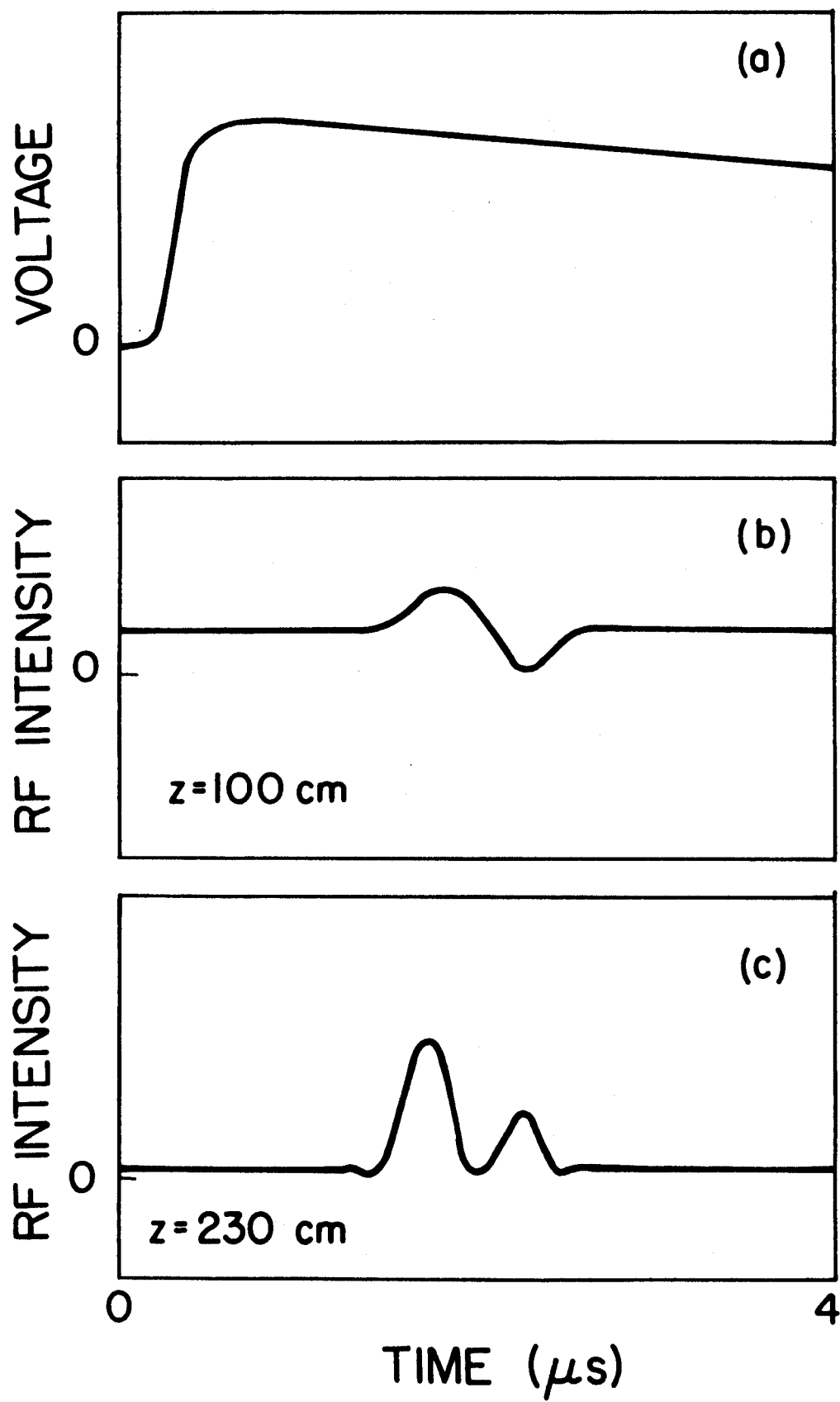
22

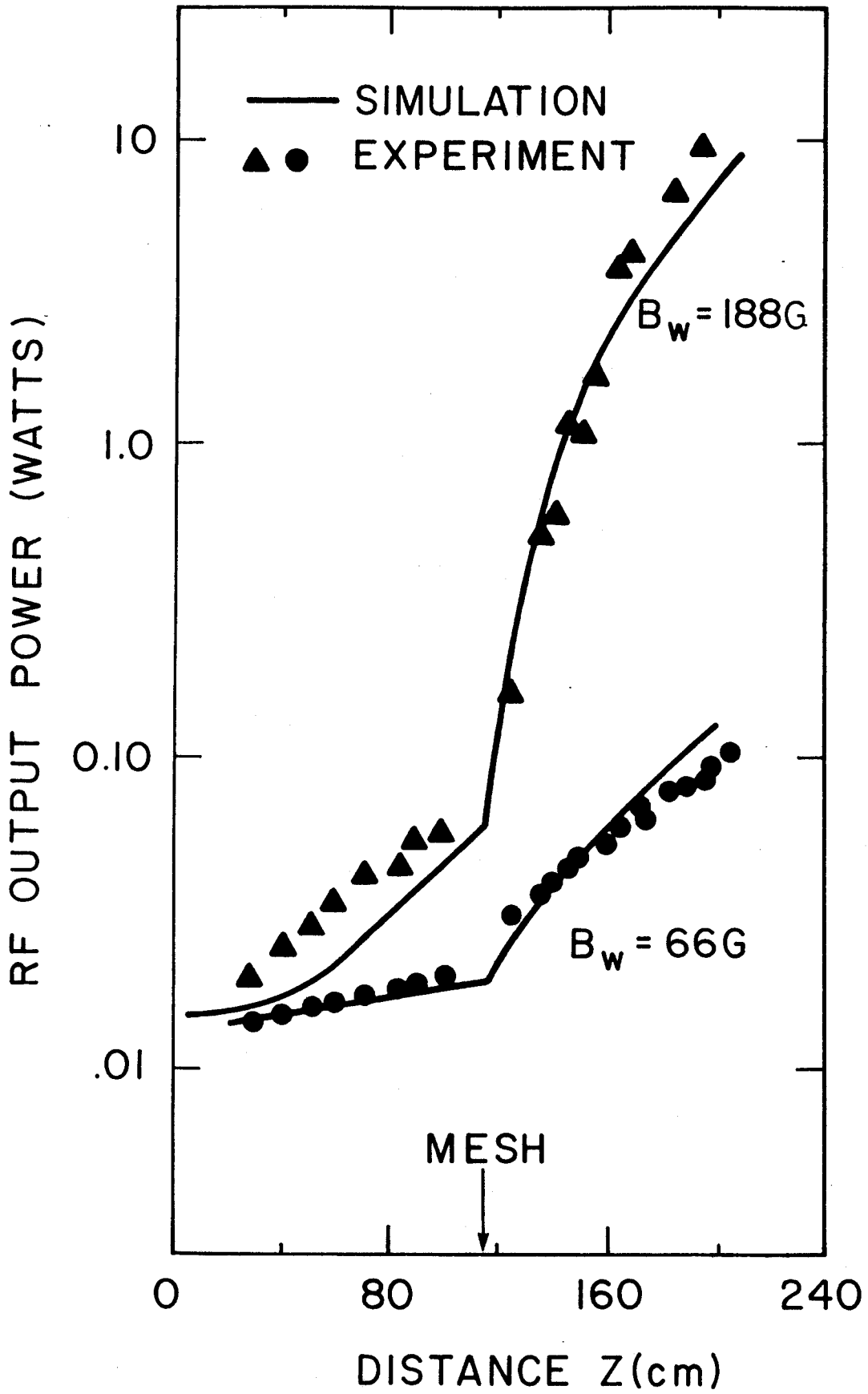in Fig. 4 decreases from left to right, which is opposite to the plot shown here.
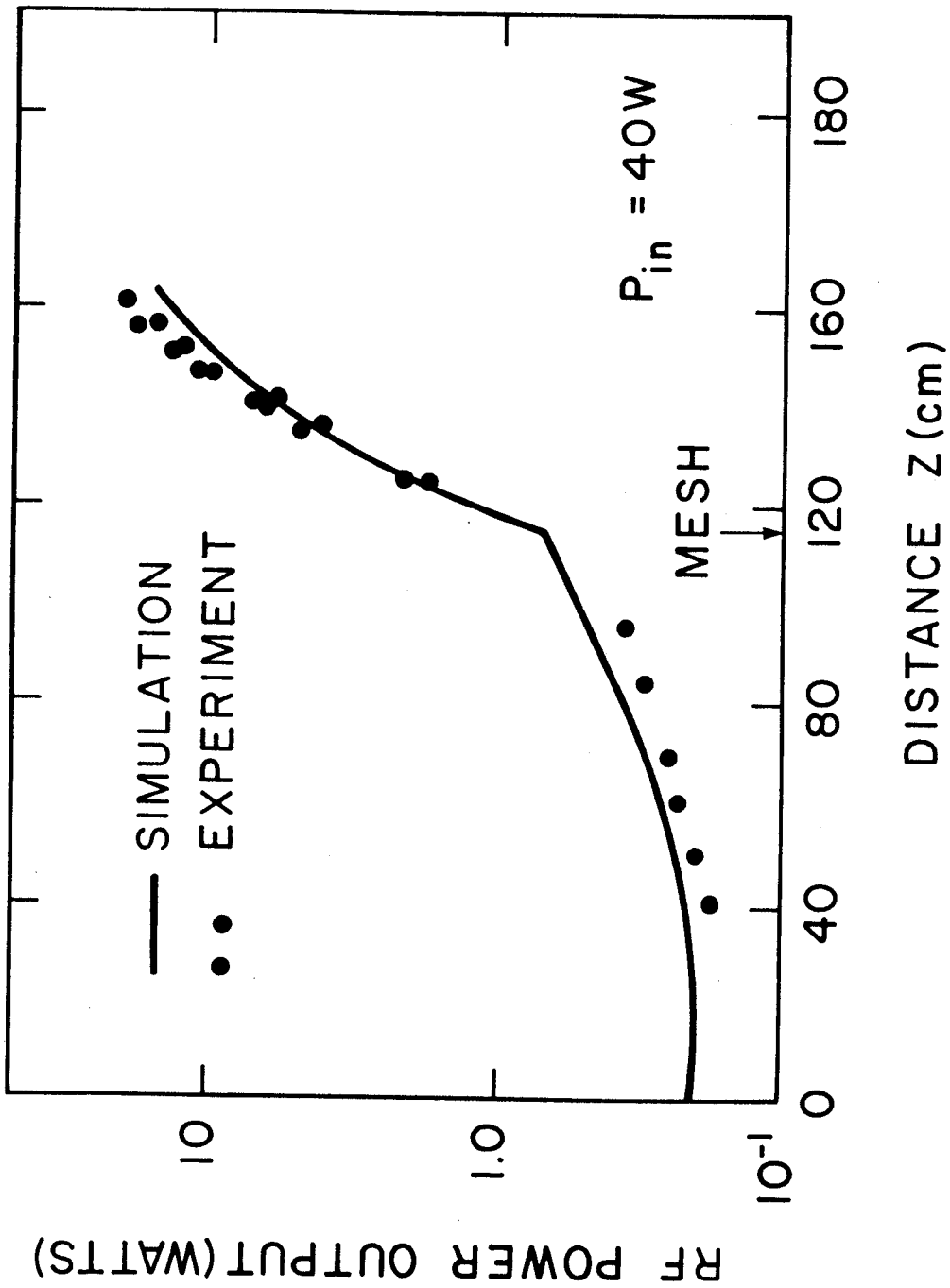
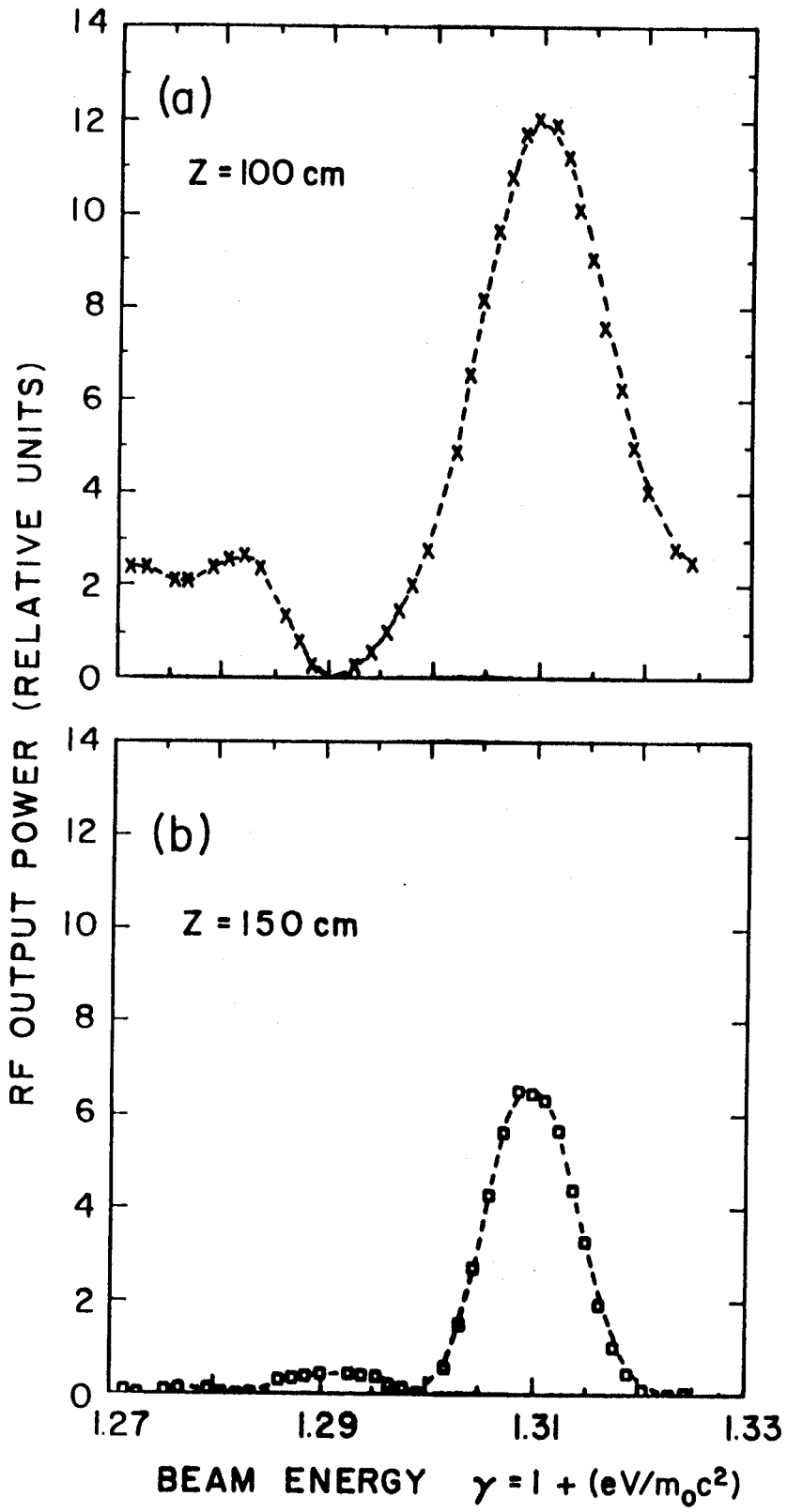Fig. 8. Comparsion between simulations and analytic results.

SOLENOID

BIFILAR HELICAL WIGGLER

RF OUTPUT POWER

WAVE LAUNCHER

TUNGSTEN MESH

225 cm

TO ACCELERATOR

FOCUSSING COILS

THERMIONIC PIERCE GUN

Fig.1 Wurtele,Bekefi,Chu,Xu

24

Fig. 2 Wurtele, Bekefi, Chu, Yu

Fig.3 Wurtele,Bekefi,Chu,Xu

(a)

VOLTAGE

0

(b)

RF INTENSITY

0

z=100 cm

(c)

RF INTENSITY

0

z=230 cm

0

TIME ($\mu$s)

4

Fig.4 Wurtele.Bekefi. Chu,Xu

Fig.6 Wurtele,Bekefi,Chu,Xu

(a)

Z = 100 cm

(b)

Z = 150 cm

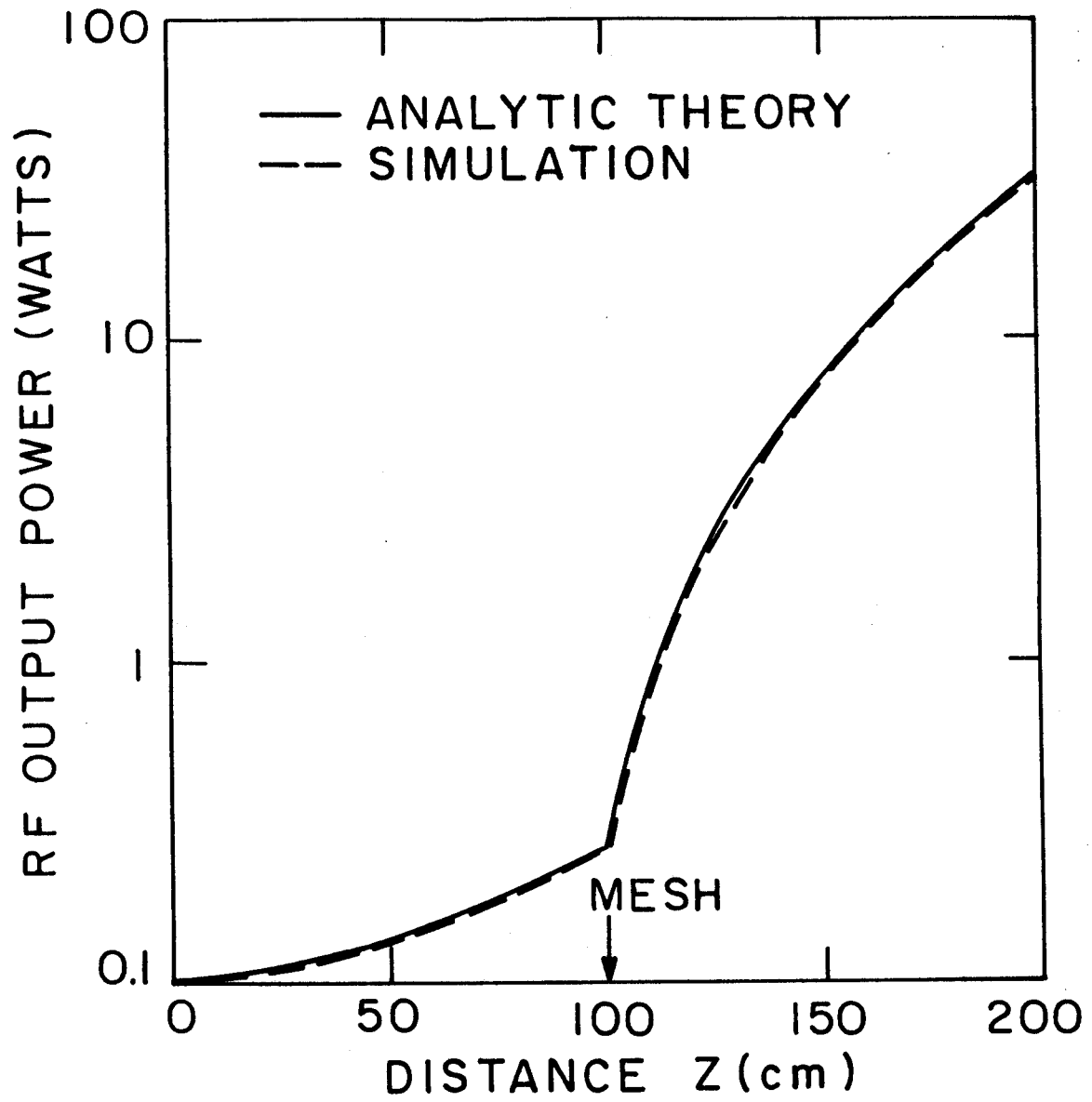RF OUTPUT POWER (RELATIVE UNITS)

BEAM ENERGY   $\gamma = 1 + (eV/m_0c^2)$

Fig.7 Wurtele,Bekefi, Chu,Xu

Fig.8 Wurtele,Bekefi, Chu,Xu